Wang, M., Lin, C.-H., and Chen, Q. 2011. "Determination of particle deposition in enclosed spaces by detached eddy simulation with the Lagrangian method," *Atmospheric Environment,* 45(30), 5376-5384.

Determination of Particle Deposition in Enclosed Spaces by Detached Eddy Simulation with the Lagrangian Method

Miao Wang[1], Chao-Hsin Lin[2] and Qingyan Chen[1,3*]

[1]School of Mechanical Engineering, Purdue University, West Lafayette, IN 47907, USA

[2]2Environmental Control Systems, Boeing Commercial Airplanes, Everett, WA 98124, USA

[3]School of Environmental Science and Technology, Tianjin University, Tianjin 300072, China

[*]Phone: (765) 496-7562, FAX: (765) 496-0539, Email: yanchen@purdue.edu

Abstract

Accurate prediction of particle deposition in airliner cabins is important for estimating the exposure risk of passengers to infectious diseases. This study developed a Detached-Eddy Simulation (DES) model with a modified Lagrangian method. The computer model was validated with experimental data for particle deposition in a cavity with natural convection and with air velocity, air temperature, and particle concentration data from a four-row, twin-aisle cabin mockup. The validation showed that the model performed well for the two cases. Then the model was further used to study particle deposition in the cabin mockup with seven sizes of particles. The particles were assumed to be released from an index passenger due to breathing or talking at zero velocity and due to coughing at a suitable jet velocity. This study can provide quantitative particle deposition distributions for different surfaces and particles removed by cabin ventilation.

Keywords: CFD, experiment, particle, deposition, indoor

Nomenclature

A	=	Model constant		N_{dA}	=	Number of particles deposited on surface area
$\overline{C}$	=	Particle deposition density		N_{total}		Total number of particles generated
C_1 , C_2 , $C_{2\varepsilon}$, C_3 , $C_{3\varepsilon}$, C_{DES}	=	Model constants		ρ , ρ_p	=	Density of air and particle

dA	=	Small surface area		S_{ij}	=	Strain rate
$\Delta_{\max}$	=	Maximum local grid spacing		σ_k	=	Model constant
ε	=	Turbulence dissipation rate		t	=	Time
$\vec{F}$	=	Other forces for particle motion		$\overline{u}, u'$	=	Mean and fluctuating air velocity
F_D	=	Drag coefficient		u^*		Friction velocity
$\vec{g}$	=	Gravitational force		$\vec{u}_p$	=	Particle velocity
G_k, G_b	=	Turbulence generation terms		x_j	=	Spatial coordinate
k	=	Turbulence kinetic energy		y^+	=	Normalized wall distance
$l_{DES}, l_{LES}, l_{rke}$	=	Length scale for DES, LES and k-ε models		Y_k	=	Dissipation term in k equation
μ, μ_t	=	Laminar and turbulence viscosity		ζ_i	=	Normal random number

1. Introduction

Over four billion people arrive at and depart from airports all over the world every year. This figure will double by 2025, according to a long term traffic forecast (ACI, 2006). Commercial airplane passengers travel in an enclosed cabin environment at close proximity (Spengler and Wilson, 2003). During the long time of air travel, the exposure risk to infectious diseases can be very high. Mangili and Gendreau (2005) evaluated the risk of infectious disease transmission in commercial airplane cabins and concluded that air travel was an important factor in the worldwide spread of infectious diseases.

Infectious disease transmission in airplane cabins can occur in many ways, such as direct contact with contagious particles generated from an infected person, inhaling pathogenic airborne agents or droplets, or touching contaminated surfaces. These different disease transmission paths are all closely related to the deposition and transport of contaminant particles or droplets. For example, saliva droplets generated by an index person through coughing or sneezing can deposit directly on the mouth or eyes of another person. The dose of airborne infectious agents and droplets is associated with their deposition rate and transport path, and a surface in an airplane cabin can be contaminated by the trapping of contaminant particles. As the commercial airplane cabins are crowded and packed with different solid surfaces, their influence on particle deposition and transport can be significant. Therefore, it is essential to evaluate the level and distribution of particle

deposition in a cabin environment.

The rapid growth of computer power makes CFD a promising tool for predicting airflows, particle transportation, and deposition in enclosed environments (Spalart and Bogue, 2003; Chen, 2008). For cabin airflow and contaminant transport simulation, Baker et al. (2006, 2008) validated their CFD prediction of air velocity and mass transport inside an aircraft cabin using measurement data. Zhang et al. (2009) measured and simulated gaseous and particulate contaminant transport in a four-row cabin mockup. Poussou et al. (2010) simulated transient flow and contaminant concentration field in a small-scale cabin mockup with a moving body. These studies explored complicated airflow and contamination concentration fields inside a cabin environment. However, particle deposition on cabin surfaces was neglected in these cases, which could be significant for a crowded cabin environment.

Particle deposition has been studied by many researchers, however, for other enclosed environments. Lai and Nazaroff (1999) applied an analogous model for particle deposition to smooth indoor surfaces and predicted a reasonable result for simple geometry. Lai and Chen (2006) conducted a Lagrangian simulation for aerosol particle transport and deposition in a chamber and found good agreement between their CFD result and the empirical estimation. Zhao et al. (2008) simulated particle deposition in ventilated rooms. Their deposition results agreed with the measured data at low turbulence level, but failed to match the experimental data when the turbulence was high. Zhang and Chen (2009) simulated particle deposition on differently oriented surfaces inside a cavity using a modified Lagrangian method and predicted improved results. Although reasonable prediction of deposition was reported by many studies, the relatively simple geometry and airflow conditions in these cases may not guarantee a good result in a much more complex environment such as an airplane cabin. A study of the literature showed that particle deposition inside an airplane cabin has not been well investigated by either numerical or experimental studies.

Using numerical simulations, this paper aims to extend the understanding of contagious particle depositions inside an airplane cabin environment. This investigation first evaluated a modified Lagrangian particle deposition model with Detached Eddy Simulation (DES) and applied it to a four-row cabin mockup. The simulation included two flow scenarios, one breathing and talking case, and the other a coughing case. The particle depositions on different cabin surfaces were determined from the simulation

results. The study discussed the deposition statistics and identified key factors related to particle depositions in airplane cabins.

2. Model formulation and verification

2.1. Modeling the airflow and turbulence

Accurate models of airflow and turbulence in an indoor environment are important for predicting the particle transportation and deposition process (Tian and Ahmadi, 2007). Many turbulence models, including RANS, LES, and DES, have been intensively tested for indoor airflow (Zhang et al., 2007). The LES and DES models showed superior overall performance over the RANS models in many benchmark tests, especially for a complicated airflow field (Wang and Chen, 2009). For a cabin simulation, LES may not be feasible since it requires very fine computational mesh near a solid wall. Alternatively, the DES model uses the RANS model in the boundary layers and LES in the main stream, which greatly reduces the computational cost of LES, while still providing comparable accuracy (Wang and Chen, 2009).

This study used the DES Realizable k-ε model (FLUENT, 2005), which can provide accurate prediction of air velocity and turbulence quantities (Wang and Chen, 2009). In addition to the continuity and momentum equations, this model calculates the turbulence by the following equations:

$$\frac{\partial}{\partial t}(\rho k)+\frac{\partial}{\partial x_j}(\rho k u_j)=\frac{\partial}{\partial x_j}\left[\left(\mu+\frac{\mu_t}{\sigma_k}\right)\frac{\partial k}{\partial x_j}\right]+G_k+G_b-Y_k \tag{1}$$

and

$$\frac{\partial}{\partial t}(\rho \varepsilon)+\frac{\partial}{\partial x_j}(\rho \varepsilon u_j)=\frac{\partial}{\partial x_j}\left[\left(\mu+\frac{\mu_t}{\sigma_\varepsilon}\right)\frac{\partial \varepsilon}{\partial x_j}\right]+\rho C_1 S\varepsilon-\rho C_2\frac{\varepsilon^2}{k+\sqrt{\nu\varepsilon}}+C_{1\varepsilon}\frac{\varepsilon}{k}C_{3\varepsilon}G_b \tag{2}$$

where:

$$C_1=\max\left[0.43,\frac{\eta}{\eta+5}\right],\eta=S\frac{k}{\varepsilon},S=\sqrt{2S_{ij}S_{ij}} \tag{3}$$

and G_k and G_b are turbulence generation due to the mean velocity gradient and buoyancy.

C_1, C_2, $C_{1\varepsilon}$ and $C_{2\varepsilon}$ are constants. The dissipation term in the k equation can be modeled as:

$$Y_k = \frac{\rho k^{3/2}}{l_{DES}} \tag{4}$$

where:

$$l_{DES} = \min\left(l_{rke}, l_{LES}\right) \tag{5}$$

and

$$l_{rke} = \frac{k^{3/2}}{\varepsilon} \tag{6}$$

$$l_{LES} = C_{DES}\Delta_{\max} \tag{7}$$

where $C_{DES} = 0.61$ is a constant, and $\Delta_{\max}$ is the maximum local grid spacing $\max\left(\Delta x, \Delta y, \Delta z\right)$.

Note that Equation (5) compares the turbulence length scale and the grid spacing. In the attached boundary layer, the turbulence length scale is smaller than the grid spacing. Equations (2) and (3) have the same form as the Realizable k-ε model, which calculates the turbulence kinetic energy and generates the "RANS-like" solution. In the fully turbulent region, the turbulence length scale is usually larger than the grid spacing. Equations (2) and (3) become the LES subgrid-scale model, which calculates the subgrid-scale turbulence kinetic energy and provides a "LES-like" solution.

2.2. Modeling Lagrangian particle motion

With the airflow information, the particle phase can be modeled by both the Eulerian and Lagrangian methods. The Eulerian method assumes the particle phase to be a continuum and calculates the particle concentration by solving a scalar transport equation. Alternatively, the Lagrangian method calculates the motion of a large number of individual particles and obtains their trajectories. Some studies from the literature have compared the two methods for particle transportation in an indoor environment (Zhang and Chen, 2006) and concluded that the Lagrangian method is more accurate and robust, especially for complex and unsteady airflow cases, which is why the Lagrangian method was applied in this study.

The Lagrangian method can be expressed as a force balance equation for an individual particle:

$$\frac{d\vec{u}_p}{dt} = F_D\left(\vec{u} - \vec{u}_p\right) + \frac{\vec{g}\left(\rho_p - \rho\right)}{\rho_p} + \vec{F} \tag{8}$$

where $\vec{u}_p$ and $\vec{u}$ are the particle and air velocities, respectively; ρ_p and ρ are the densities of particles and air respectively; $\vec{g}$ is the gravitational force; $\vec{F}$ is other forces considered in the simulation, including the Thermophoretic force, Saffman lift force, and Brownian force; and F_D is the drag coefficient. Due to the limited space available in this paper, the formulations of $\vec{F}$ and F_D are not included, but can be found in the literature (FLUENT, 2005).

2.3. Modeling particle turbulence dispersion and deposition

Particle deposition occurs within a thin layer near the wall (Lai and Chen, 2006), where the mean airflow velocity is zero in the wall-normal direction due to the no-slip boundary condition. However, the turbulence velocity component may not be zero and is a key factor for particle deposition. Therefore, it is essential to correctly model the turbulence velocity component, especially near the wall.

In Equation (8), the term $\vec{u}$ represents the actual airflow velocity, which should be obtained by solving the airflow models. However, the airflow solution provided by the DES model may not be sufficient. In the attached boundary layer, where the DES model switches to RANS mode, the velocity can be written as:

$$\vec{u} = \bar{u} + u' \tag{9}$$

where $\bar{u}$ is the "RANS-like" mean velocity solved by the DES model, u' turbulence velocity component that should be properly modeled.

In the core turbulence region, the DES model switches to LES mode. The air velocity has the same form as Equation (9) except the term $\bar{u}$ is the "LES-like" velocity field resolved by the DES model, and u' represents the subgrid-scale turbulence fluctuation, which

should also be modeled.

The turbulence dispersion and deposition can be modeled by the Discrete Random Walk (DRW) model as:

$$u_i^{'} = \zeta_i \sqrt{2k/3} \tag{10}$$

where k is the turbulence kinetic energy in the RANS region and the subgrid-scale turbulence kinetic energy in the LES region. ζ_i is a normal random number (FLUENT, 2005).

This model relates the fluctuating air velocity at the particle to the value of the (subgrid-scale) turbulence kinetic energy in the center of the computational cell in which the particle is located. This assumption holds if a particle is far from solid walls, where the variation in turbulence kinetic energy within one cell is negligible. However, in a wall-adjacent cell, the turbulence kinetic energy decreases to zero all the way from the cell center to the wall. For a near-wall particle, Equation (10) may overpredict the fluctuating velocity component, thus causing overprediction of the particle deposition (Matida et al., 2000).

To correctly predict the fluctuating velocity for the near wall particles, a deposition model should be applied. Although there is no deposition model available for the DES models, many models have been developed for different RANS models, which may be used by the DES in its near wall region. He and Ahmadi (1999) assumed the quadratic variation of normal Reynolds stress and developed a deposition model for the Reynolds stress turbulence model. Zhang and Chen (2009) applied the v2f turbulence model and used the v2 value as the wall normal fluctuation to account for the near wall damping effect. These two models correctly modeled the near wall behavior and generated a reasonable particle deposition result. However, these models are only valid for the turbulence models for which they were developed. For the k-ε family models, Matida et al. (2004) used the dumping function proposed by Wang and James (1999) for all velocity components. Lai and Chen (2006) combined the methods of Matida et al. (2004) and He and Ahmadi (1999) and developed a deposition model with a more concise formulation:

$$u_i^{'} = \begin{cases} \zeta_i A u^* y^{+2} & y^+ \le 4 \\ \zeta_i \sqrt{2k/3} & y^+ > 4 \end{cases} \quad (11)$$

where $A = 0.008$ is a constant proposed by Bernard and Wallace (2002), u^* is the shear velocity, and y^+ is the distance from a particle to the nearest wall in the wall unit.

Equation (11) has the same form as Equation (10) if $y^+ > 4$ and only applies the correction in the near wall region. Note that near the wall, this model uses a correlation instead of the cell center value for the turbulence kinetic energy and thus does not require a refined near wall mesh. In this study, this model was applied with the DES Realizable k-ε model to calculate the particle deposition.

2.4. Model verification

This study first validated the DES model with the dispersion and deposition model by simulating the particle deposition in a cavity with natural convection (Thatcher et al., 1996). Figure 1 shows the schematic of the cavity, which was a cubic chamber with a floor and a heated wall, as well as a ceiling and a cooled wall. The front and back walls were well insulated and adiabatic. This setting generated a counter-clockwise circulation in the room. Particles of five different sizes were released at the center of the cavity, and gradually mixed with the air in the cavity. Their deposition was measured at four differently oriented surfaces.

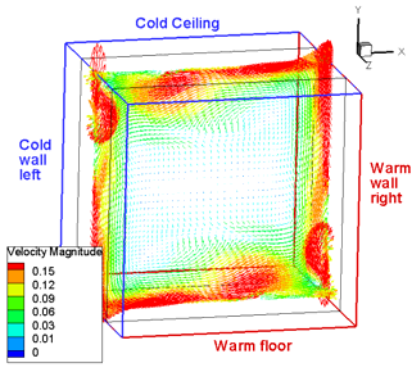

Figure 1 Schematic and the flow pattern of the inside of the cavity with natural convection (Thatcher et al. 1996).

The numerical simulation was based on ANSYS FLUENT (version 12.1). The computational mesh contained 262,144 hex cells (64x64x64) with a refined boundary layer. The DES Realizable k-ε model was applied together with the modified DRW model.

Figure 2 compares the predicted and measured particle deposition velocity on the four surfaces. With the DES model, the modified DRW model predicted reasonable results at the ceiling, floor, and cold wall, but overpredicted the deposition velocity at the warm wall, which was also found by Zhang and Chen (2009). When used with RANS model (RNG k-ε), the modified DRW model showed similar performance. Without the near wall modification, the standard DRW model with DES model overpredicted the deposition velocity by two orders of magnitude. This was because the near wall grid size was much larger than the particle size. The turbulence dispersion evaluated at the cell center may be too large if a particle is close to the wall. In general, the modified DRW model showed significant improvement over the standard DRW model and will be used in the following simulation.

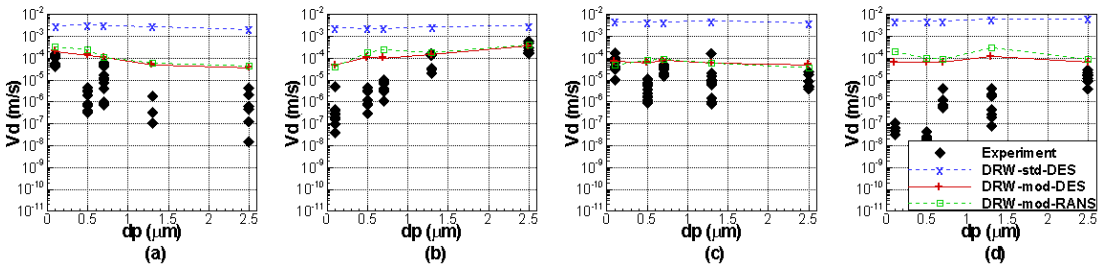

Figure 2 Comparison of predicted and measured particle deposition velocity on different surfaces: (a) ceiling, (b) floor, (c) cool wall, (d) warm wall.

3. Prediction of particle deposition in a four-row airplane cabin

The DES Realizable k-ε model with the modified DRW model has been applied to the study of the particle deposition in a full-scale four-row cabin mockup. Detailed experimental data on airflow velocity and particle concentration (Zhang et al., 2009) was available for further model verification. This study was also modified to study particle deposition from the breathing and coughing of a passenger.

3.1. Case description

Figure 3 depicts the schematic of the four-row twin-aisle cabin mockup. In the experiment (Zhang et al., 2009), the cabin mockup had 28 seats, 14 of which were occupied by human simulators, as shown in red in the figure. The air was supplied from two groups of linear diffusers located near the center of the ceiling. The total airflow rate was 0.23 m^3/s, or 8.2 L/s per passenger seat. Three-dimensional air velocity and air temperature were measured at two planes, as depicted in green in Figure 3. The air velocity and temperature profiles at the inlet diffuser and the temperature of different surfaces were also measured.

The particle source was located at the center seat of the third row (seat 3D), as shown in Figure 3. Non-evaporative, monodispersed Di-Ethyl-Hexyl-Sebacat (DEHS) particles were released from the source into the cabin with a small momentum. After the airflow and particle field reached a steady-state, the particle concentration was measured at eight positions, as shown in Figure 3. The particle used in the experiment had a diameter of 0.7μm. However, in the CFD simulation, seven sizes of particles (0.1, 0.7, 2.5, 5, 10, 20, and 100μm) were simulated to study the influence of particle size on the particle deposition.

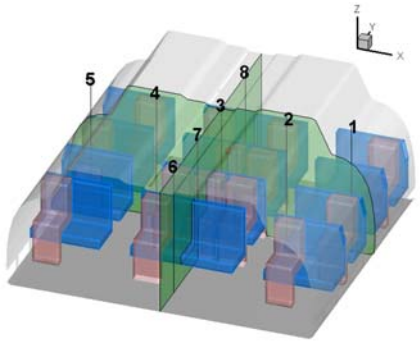

Figure 3 Schematic of the four-row cabin mockup (Zhang et al. 2009).

The numerical simulation was conducted based on CFD code ANSYS FLUENT (version 12.1). The study applied the DES Realizable k-ε model with the modified Lagrangian method as discussed before. The simulation used a solution from the RNG k-ε model as the initial field and calculated 10 minutes of flow time to reach the steady-state flow field. Then, the particles were continuously released from the source into the cabin and were mixed with the cabin air. For each particle size, 1000 particles were generated every second. The particle concentration at seats 1A, 1D, 3D and 4D, and the total number of particles in the cabin were monitored during the calculation. The case was calculated for

another 15 minutes (six complete air changes) of flow time until the particle concentration field reached steady-state, when the monitored values became stable. The averaged air velocity, particle concentration, and deposition results were obtained in the next five minutes of flow time.

3.2. Air velocity and particle concentration field

Figure 4 compares the simulated (DES and RNG k-ε) and measured air velocity vectors at the cross-section through the third row and at the mid-section along the longitudinal direction. In the cross-sectional view (Figure 4 (a)), the ceiling diffusers and the thermal plume in the middle generated two large circulations at each side of the cabin. The DES prediction agreed with the measurement in terms of circulation pattern. But significant discrepancies can be found in a quantitative comparison. The result from the RNG k-ε model was comparable with the DES result, which was also reported by Zhang et al. (2009), who further concluded that the simulation was very sensitive to the accuracy of the boundary conditions. In the experiment, the velocity magnitude was accurately measured, while the direction was not, which generated error for quantitative comparison, but still preserved qualitative character of the velocity field. Note that the airflow field was asymmetrical due to the inlet and wall-boundary conditions.

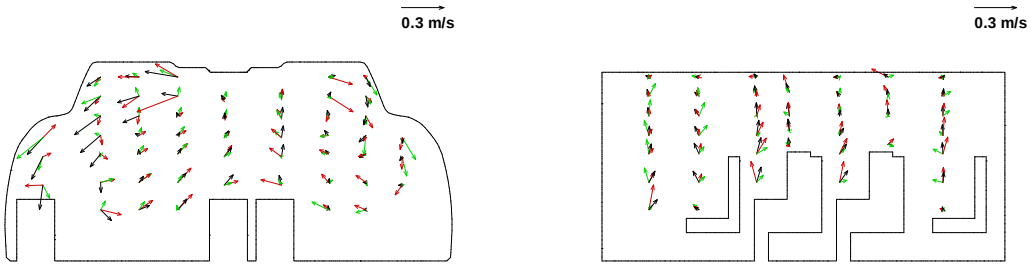

(a) (b)

Figure 4 Comparison of simulated (black vectors for DES, and green vectors for RNG k-ε) and measured (red vectors) airflow field at: (a) the cross-section through the third row, and (b) the mid-section along the longitudinal direction.

In the mid-section along the longitudinal direction, the vector field shows an upward motion due to the two circulations and the thermal plume in the middle of the cabin. The DES result agreed reasonably well with the measured data as shown in Figure 4 (b), though differences can be found at some positions. For example, at the third row, the DES model predicted a backward airflow motion, which was not supported by the

measurements. At the same location, the DES results also predicted a smaller upward velocity than did the experiment. Comparing with the DES model, the RNG k-ε model predicted larger errors in this section. For such a complex case, a DES model may be more suitable than the RANS models.

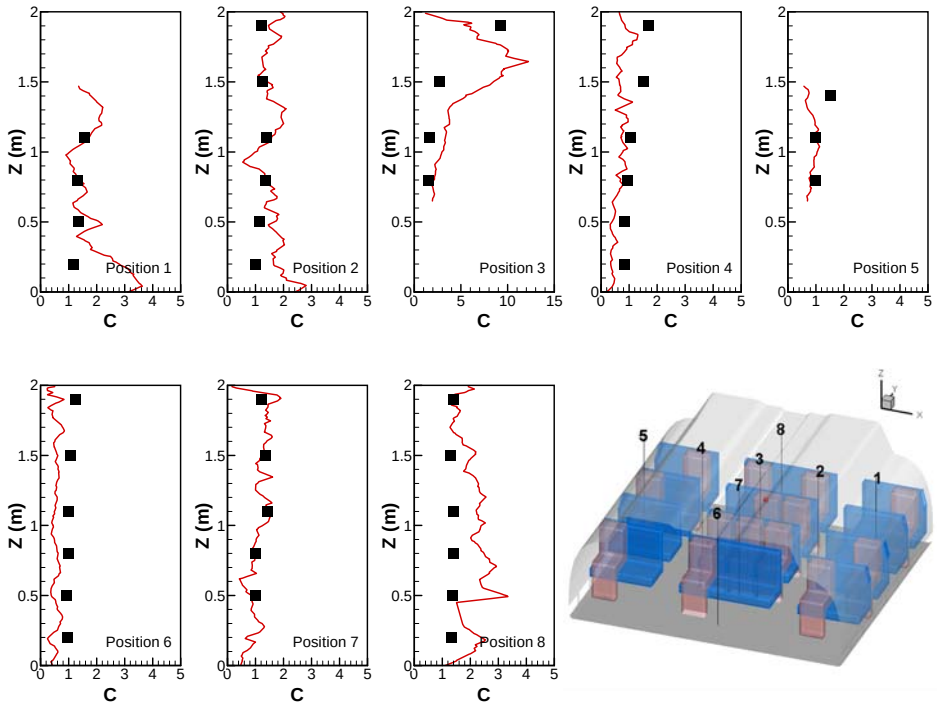

Figure 5 Comparison of the measured (symbols) and predicted (lines) particle concentration profiles in different positions ($C = C_{local}/C_{exhaust}$).

Figure 5 compares the simulated and measured concentrations for particles with 0.7 μm diameter at eight different positions. In general, the DES model predicted reasonably good results. At position 3 where the source was located, the DES model predicted a correct shape and magnitude of the concentration peak. However, the peak was slightly shifted down due to the underpredicted upward velocity. Far from the particle source, the particle concentration was approximately in a well-mixed condition, which was nicely captured by the DES model. However at position 8, the DES model overpredicted the concentration level due to the erroneous backward airflow prediction. For the same reason, the concentration at position 6 was underpredicted. At position 4, the particle concentration was underpredicted especially near the ceiling due to the incorrect airflow prediction closed to the ceiling diffuser. Note that, the predicted concentration profile shows fluctuation due to the discrete nature of the Lagrangian method, which was also

observed by Zhang et al., (2009). Since the air temperature is not essential for particle deposition and the space of this paper is limited, this paper did not show validation for the air temperature. However, good agreement was found between the predicted and measured air temperature field.

3.3. Particle deposition onto different surfaces

3.3.1. Breathing and talking

In the experiment, the particles were released with a jet flow of velocity magnitude equal to 1 m/s, which could be representative of the particle release from the breathing (2.5 m/s) or talking (1.1 m/s) of a passenger (Gupta et al., 2010). The distribution of the particle deposition at solid walls and exhaust vents was also calculated for five minutes of flow time in this investigation. The particle deposition density was calculated as:

$$\overline{C} = \frac{N_{dA}}{N_{total} \cdot dA} \tag{11}$$

where N_{dA} was the number of particles deposited on surface area, dA, during a certain amount of time; N_{total} was the total number of particles generated during the same time; and dA was a small surface area, which was the same as the local computational mesh.

This study simulated the particle deposition with seven different particle sizes, which can be divided into three groups: small particles (0.1, 0.7 and 2.5μm), medium particles (5, 10 and 20μm), and large particles (100μm). Due to the limited space available, this paper only shows results for the 0.7, 10, and 100 μm particles to represent each category.

Figure 6 shows the particle deposition density of the 0.7, 10, and 100 μm particles. Due to the asymmetrical airflow pattern, the deposition was also asymmetrical. For the small (0.7 μm) particles, a high particle deposition density was observed at the ceiling and side walls along the path of the major circulation (Figure 6(a)), while the floor and seat had relatively low particle deposition density (Figure 6(d)). This is because the particles were small and they mainly followed the airflow pattern. The small 0.7 μm particles were carried by the thermal plume to reach the ceiling, where most particles joined the airflow circulation formed by the supply jets. The particles deposited at the ceiling and side walls along their path to the exhaust.

For the medium (10 μm) particles, Figure 6(b) shows that their deposition at the ceiling and side walls was similar to that of the small particles, but the deposition rate was much lower. The particle deposition density at the floor was higher. As the particle size increased, the gravitational force became comparable to the drag force, which changed the deposition distribution.

For the large (100 μm) particles, Figure 6(c) shows no deposition on the ceiling and side walls. All the particles were deposited at the surfaces of passenger 3D, as shown in Figure 6(f). For particles of this size, the gravitational force was dominant. The particles had a free fall motion from its source (mouth/nose) and deposited within a very small area on passenger 3D.

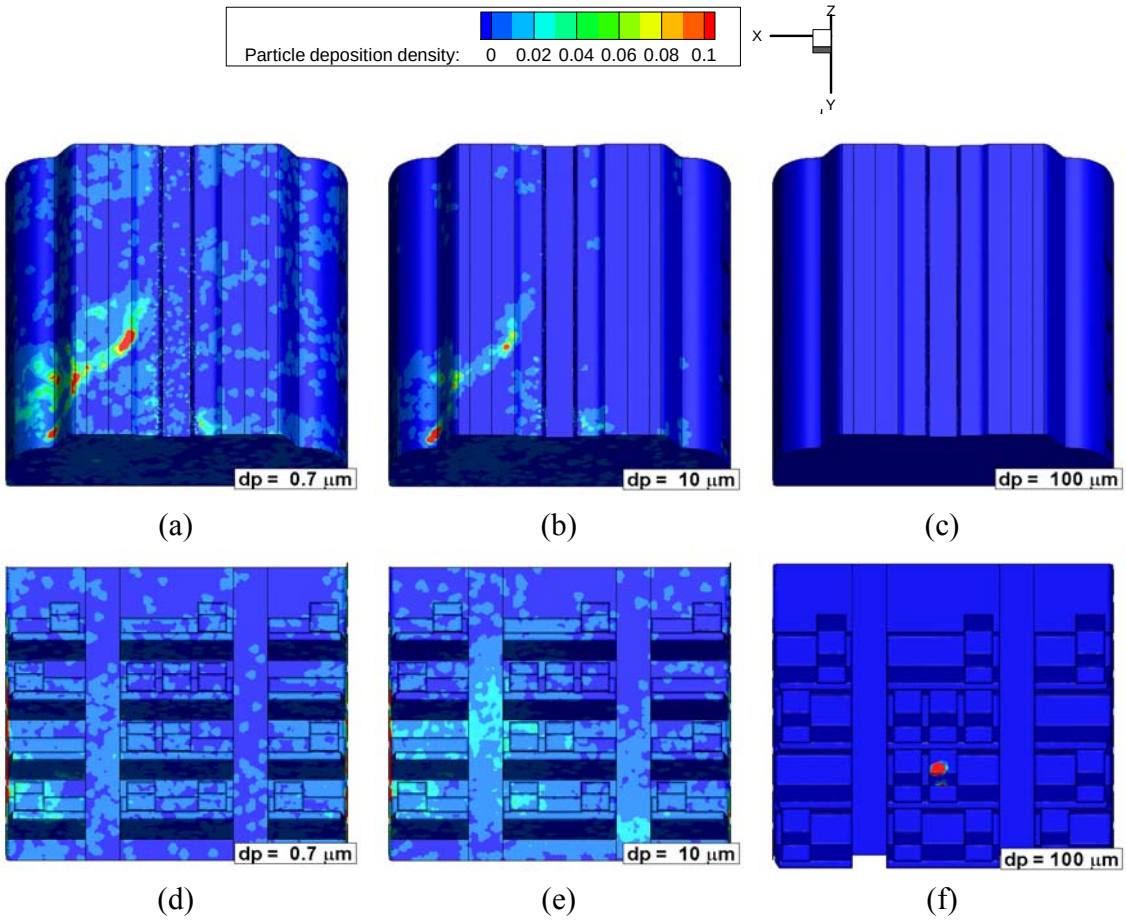

Figure 6 Particle depositions at different surfaces for the breathing and talking case: the top row is for the ceiling and side wall surfaces and the bottom row for the floor and seats surfaces (a) and (d) for 0.7 μm particles, (b) and (e) for 10 μm particles, and (c) and (f) for 100 μm particles.

3.3.2. Coughing

This study further modified the initial conditions for the particles so as to study the particle deposition with a cough from a passenger. As suggested by Gupta et al. (2009), the coughing jet was injected from the mouth of the passenger 3D with area of opening of 4 cm^2, and air velocity of 11.5 m/s. The direction of the jet flow was 22.5 degree downward along the -y direction. As in the previous case, seven sizes of particles were continuously released from the cough by the passenger at seat 3D. All the models and simulation procedures were the same as in the breathing and talking case.

Figure 7(a) shows the particle deposition density of the 0.7 μm particles at the ceiling and side walls. Compared with the previous case, the deposition on the ceiling and side walls was significantly reduced. This was because the jet flow that carried the particles could penetrate the thermal plume. Therefore, most of the particles did not enter the major circulation so they could not reach the ceiling. For the deposition on the floor and seats, Figure 7(d) shows a high particle deposition density on the seat back of passenger 2D, the surface of passenger 3D, and the floor area close to seat 3D, due to the jet impingement.

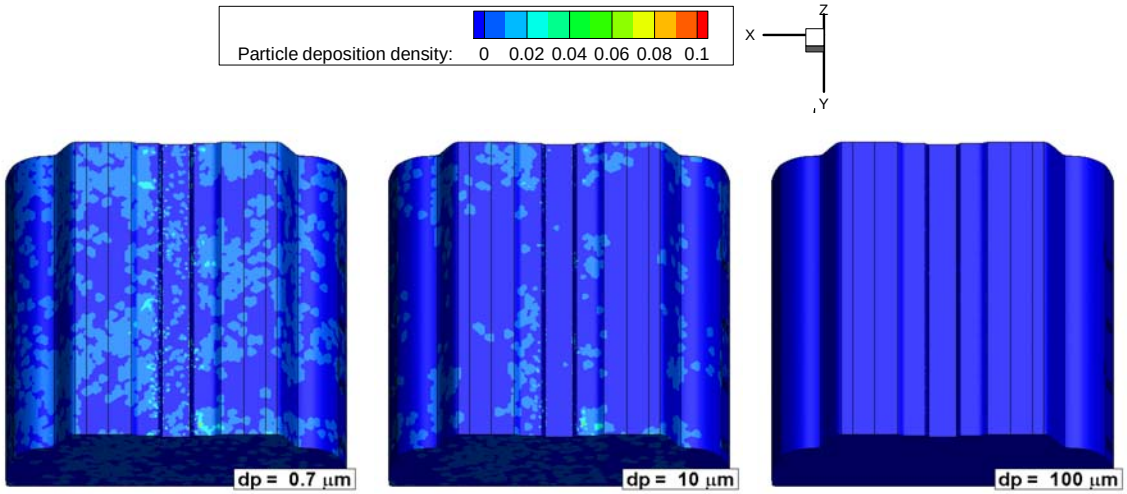

(a) (b) (c)

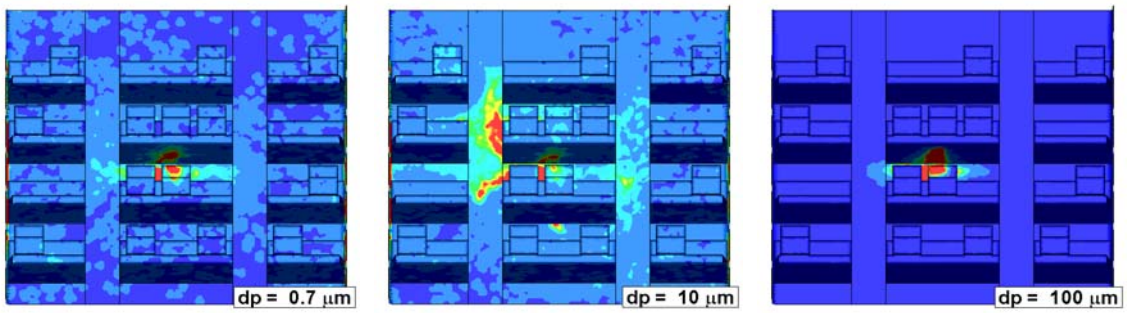

(d) (e) (f)

Figure 7 Particle depositions at different surfaces for the coughing case: the top row is for the ceiling and side wall surfaces and the bottom row is for the floor and seats surfaces (a) and (d) for 0.7 μm particles, (b) and (e) for 10 μm particles, and (c) and (f) for 100 μm particles.

For the 10 μm particles, Figure 7(b) shows a lower particle deposition density at the ceiling and side walls than that for the breathing and talking case. As shown in Figure 7(e), a high particle deposition density was observed in the areas of jet impingement. Unlike the 0.7 μm particles that mostly suspended in the air after entering the air, a majority of the 10 μm particles deposited due to the jet momentum and the gravity.

For the 100 μm particles, Figure 7(c) shows that no particles deposited on the ceiling and side walls. All the particles deposited on the back surface of seat 2D, the surface of passenger 3D, and the floor close to seat 3D due to direct impingement and gravity because these particles were too heavy to be carried by the airflow.

4. Discussion

The previous section discussed the distribution of particle deposition. For assessing the infection risk, it is also essential to count the number of particle depositions on different surfaces, especially at the surfaces in close proximity to the passengers. This investigation first classified all surfaces into nine categories based on their locations, properties, and functions. As shown in Figure 8, the nine types of surfaces included: exhaust, passengers, floor, ceiling, side walls, section ends, seat back, seat front, and tray tables.

Figure 9 shows the statistics of the particle deposition on different types of surfaces. For the breathing and talking case (Figure 9 (a)), 65% of the 0.7 μm particles were removed by air through the exhaust. The side walls and ceiling trapped a large portion of the

particles (12% and 8%, respectively). These surfaces may not be frequently contacted by passengers. The passenger surfaces had 7% of the 0.7 μm particles. Despite the large area, the floor only received 3% of the particles. The two section ends trapped 2% of the particles because the airflow along the longitudinal direction was small. The seat front, seat back, and tray tables trapped 3% of the particles that could likely be touched by the passengers. For the 10 μm particles as shown in Figure 9(b), the number of particles exhausted was reduced to 55%, but was still a majority. The deposition on the ceiling decreased to 2% since gravity became important for this size of particle. For the 100 μm particle as shown in Figure 9(c), 100% of the particles deposited on the surface of the index passenger, which can be explained by their free fall motion. In general, the gravity force played a major role in the particle deposition.

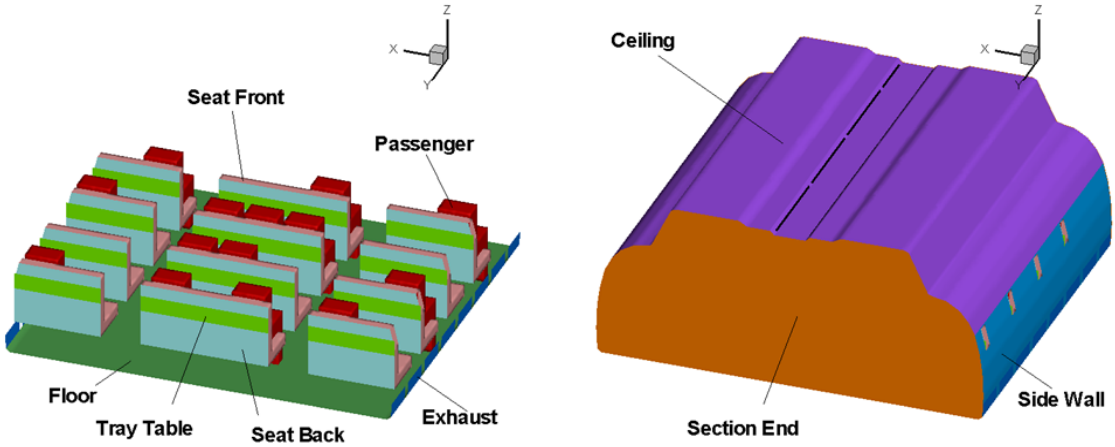

Figure 8 Definitions of the nine different types of surfaces.

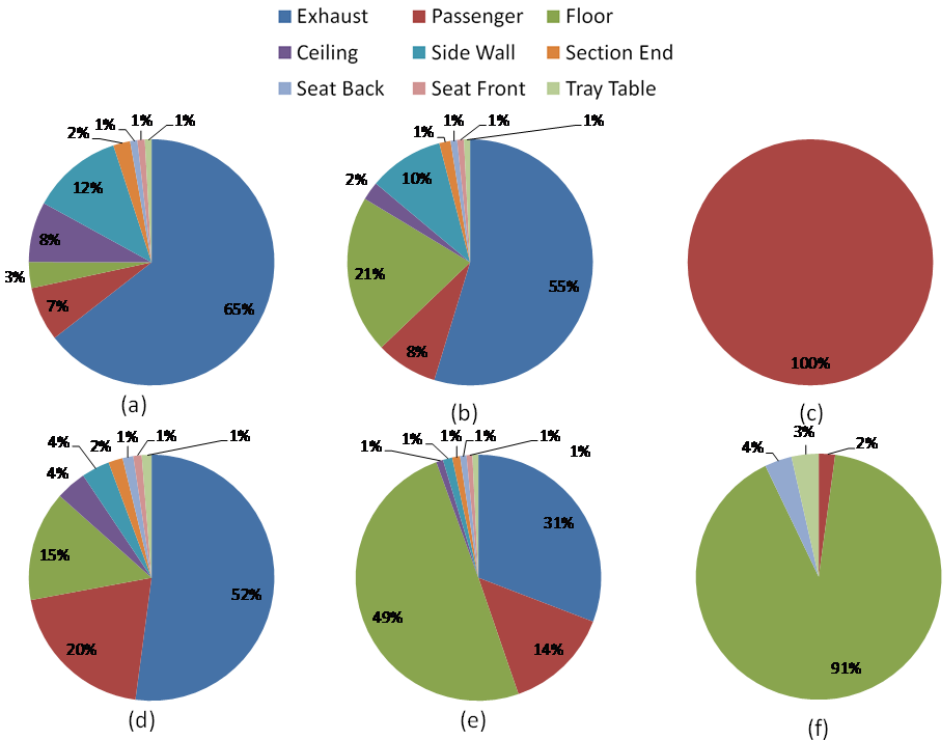

Figure 9 Statistics of particle deposition on different types of surfaces: (a) 0.7 μm particles in the breathing case, (b) 10 μm particles in the breathing case, (c) 100 μm particles in the breathing case, (d) 0.7 μm particles in the coughing case, (e) 10 μm particles in the coughing case, and (f) 100 μm particles in the coughing case.

In the coughing case, the jet could penetrate the thermal plumes and could transport the particles to the lower part of the cabin. The jet impingement enhanced particle deposition on the floor, thus increasing the total particle deposition by 13% and 14% for the 0.7 μm and the 10 μm particles, respectively, as shown in Figures 9(d) and 9(e). For the two particle sizes, the deposition on the passenger also increased. The deposition on the ceiling and side walls decreased slightly. As shown in Figure 9(f), 91% of the 100 μm particles deposited on the floor, with the rest on the seat back and tray table in front of the index passenger.

5. Conclusion

This study applied the DES model with a modified Lagrangian method to predict the particle dispersion in a cavity with natural convection and in a four-row airplane cabin mockup. By comparing with the experimental data, this investigation found that this new model can predict reasonably good results for air velocity, particle concentration, and particle deposition for the two cases.

For the cabin case, seven sizes of particles were assumed to be released by an index passenger sitting in the middle of the cabin due to breathing with zero velocity and due to coughing with suitable jet velocity. This study found that the distribution of particle deposition onto surfaces depended on particle size, particle release mode, and the airflow pattern in the cabin. In the breathing case, 35% of the small (0.7μm) particles, 55% of the medium (10μm) particles, and 100% of the large (100μm) particles deposited onto the cabin surface and the rest were removed by the cabin ventilation. In the coughing case, the number of small, medium and large particles particles deposited changed to 48%, 69%, and 100%, respectively.

References

ACI. The Global Airport Community, 2007. www.airports.org/aci/aci/file/Annual Report/ACI Annual Report 2006 FINAL.pdf

Baker, A. J., Ericson S.C., Orzechowski, J.A., Wong K.L. and Garner, R.P., 2006. Aircraft passenger cabin ECS-generated ventilation velocity and mass transport CFD simulation: Velocity field validation. Journal of the IEST (Online) 49(2), 51-83.

Baker, A. J., Ericson S.C., Orzechowski, J.A., Wong, K.L. and Garner, R.P., 2008. Aircraft passenger cabin ECS-generated ventilation velocity and mass transport CFD simulation: Mass transport validation exercise. Journal of the IEST (Online) 51(1), 90-113.

Bernard, P. S., and Wallace, J. M., 2002. Turbulent flow: Analysis, measurement and prediction, New Jersey: Wiley.

Chen, Q., 2008. Ventilation performance prediction for buildings: A method overview and recent applications. Building and Environment 44(4), 848-58.

FLUENT, 2005. Fluent 6.2 Documentation. Fluent Inc., Lebanon, NH.

Gunther, G., Bosbach, J., Pennecot, J., Wagner, C., Lerche, T. and Gores, I., 2006. Experimental and numerical simulations of idealized aircraft cabin flows. Aerospace Science and Technology 10(7), 563-573.

Gupta, J.K., Lin, C.-H. and Chen, Q., 2009. Flow dynamics and characterization of a cough. Indoor Air 19, 517-525.

Gupta, J.K., Lin, C.-H., and Chen, Q., 2010. Characterizing exhaled airflow from breathing and talking. Indoor Air 20, 31-39.

He, C. and Ahmadi, G., 1999. Particle deposition in a nearly developed turbulent duct flow with electrophoresis. Journal of Aerosol Science 30, 739-758.

Lai, A. C. K. and Nazaroff, W.W., 2000. Modeling indoor particle deposition from turbulent flow onto smooth surfaces. Journal of Aerosol Science 31, 463-476.

Lai A. C. K. and Chen F., 2006. Modeling of particle deposition and distribution in a chamber with a two-equation Reynolds-averaged Navier–Stokes model. Journal of Aerosol Science 37(12), 1770-80.

Mangili, A. and Gendreau, M.A., 2005. Transmission of infectious diseases during commercial air travel. Lancet 365, 989-996.

Matida, E. A., Nishino, K. and Torii, K., 2000. Statistical simulation of particle deposition on the wall from turbulent dispersed pipe flow. International Journal of Heat and Fluid Flow 21, 389-402.

Matida, E. A., Finlay, W. H., Lange, C. F. and Grgic, B., 2004. Improved numerical simulation of aerosol deposition in an idealized mouth–throat. Journal of Aerosol Science 35, 1-19.

Poussou, S., Mazumdar, S., Plesniak, M.W., Sojka, P. and Chen, Q., 2010. Flow and contaminant transport in an airliner cabin induced by a moving body: Scale model experiments and CFD predictions. Atmospheric Environment 44(24), 2830-2839.

Spalart, P. R. and Bogue, D. R., 2003. The role of CFD in aerodynamics, off-design. Aeronautical Journal 107(1072), 323-329.

Spengler, J. D. and Wilson, D. G., 2003. Air Quality in Aircraft, Proceedings of the Institution of Mechanical Engineers, Part E: Journal of Process Mechanical Engineering 217, 323-335.

Thatcher, T.L., Fairchild, W.A. and Nazaroff, W.W., 1996. Particle deposition from natural convection enclosure flow onto smooth surfaces. Aerosol Science and Technology 25, 359-374.

Tian, L. and Ahmadi, G., 2007. Particle deposition in turbulent duct flows - comparisons of different model predictions. Journal of Aerosol Science 38, 377-397.

Wang, M. and Chen, Q., 2009. Assessment of various turbulence models for transitional flows in enclosed environment, HVAC&R Research 15(6), 1099-1119.

Wang, Y. and James, P. W., 1999. On the effect of anisotropy on the turbulent dispersion and deposition of small particles. International Journal of Multiphase Flow 5, 551-558.

Zhang, Z. and Chen, Q., 2006. Experimental measurements and numerical simulations of particle transport and distribution in ventilated rooms. Atmospheric Environment 40(18), 3396-3408.

Zhang Z, Zhai ZQ, Zhang W, Chen Q., 2007. Evaluation of various turbulence models in predicting airflow and turbulence in enclosed environments by CFD: Part

2-comparison with experimental data from literature. HVAC&R Research 13(6):871-886.

Zhang, Z. and Chen, Q., 2009. Prediction of particle deposition onto indoor surfaces by CFD with a modified Lagrangian method. Atmospheric Environment 43(2), 319-328.

Zhang, Z., Chen, X., Mazumdar, S., Zhang, T. and Chen, Q., 2009. Experimental and numerical investigation of airflow and contaminant transport in an airliner cabin mockup. Building and Environment 44(1), 85-94.

Zhao B., Yang C., Yang X. and Liu S., 2008. Particle dispersion and deposition in ventilated rooms: Testing and evaluation of different Eulerian and Lagrangian models. Building and Environment 43(4), 388-97.